
















Planet Search with the Keck/NIRC2 Vortex Coronagraph in M_s -band for Vega

Bin B. Ren (任彬) ^{1,2,3}, Nicole L. Wallack ^{4,5}, Spencer A. Hurt ⁶, Dimitri Mawet ^{3,7}, Aarynn L. Carter ⁸, Daniel Echeverri ³, Jorge Llop-Sayson ³, Tiffany Meshkat ⁹, Rebecca Oppenheimer ¹⁰, Jonathan Aguilar ¹¹, Eric Cady ⁷, Élodie Choquet ¹², Garreth Ruane ⁷, Gautam Vasisht ⁷, and Marie Ygouf ⁷

¹ Université Côte d’Azur, Observatoire de la Côte d’Azur, CNRS, Laboratoire Lagrange, F-06304 Nice, France; e-mail: bin.ren@oca.eu

² Univ. Grenoble Alpes, CNRS, IPAG, F-38000 Grenoble, France

³ Department of Astronomy, California Institute of Technology, MC 249-17, 1200 East California Boulevard, Pasadena, CA 91125, USA

⁴ Earth and Planets Laboratory, Carnegie Institution for Science, Washington, DC 20015, USA

⁵ Division of Geological & Planetary Sciences, California Institute of Technology, MC 150-21, 1200 East California Boulevard, Pasadena, CA 91125, USA

⁶ Department of Earth Sciences, University of Oregon, Eugene, OR 97403, USA

⁷ Jet Propulsion Laboratory, California Institute of Technology, 4800 Oak Grove Drive, Pasadena, CA 91109, USA

⁸ Department of Astronomy & Astrophysics, University of California, Santa Cruz, 1156 High St, Santa Cruz, CA 95064, USA

⁹ Infrared Processing and Analysis Center (IPAC), California Institute of Technology, MC 100-22, 1200 East California Boulevard, Pasadena, CA 91125, USA

¹⁰ American Museum of Natural History, New York, NY 12345, USA

¹¹ Space Telescope Science Institute (STScI), 3700 San Martin Drive, Baltimore, MD 21218, USA

¹² Aix Marseille Univ, CNRS, CNES, LAM, Marseille, France

Received 12 July 2022 / Revised 17 January 2023 / Accepted 18 January 2023

ABSTRACT

Context. Gaps in circumstellar disks can signal the existence of planetary perturbers, making such systems preferred targets for direct imaging observations of exoplanets.

Aims. Being one of the brightest and closest stars to the Sun, the photometric standard star Vega hosts a two-belt debris disk structure. Together with the fact that its planetary system is being viewed nearly face-on, Vega has been one of the prime targets for planet imaging efforts.

Methods. Using the vector vortex coronagraph on Keck/NIRC2 in M_s -band at $4.67 \mu\text{m}$, we report the planet detection limits from 1 au to 22 au for Vega with an on-target time of 1.8 h.

Results. We reach a $3 M_{\text{Jupiter}}$ limit exterior to 12 au, which is nearly an order of magnitude deeper than existing studies. Combining with existing radial velocity studies, we can confidently rule out the existence of companions more than $\sim 8 M_{\text{Jupiter}}$ from 22 au down to 0.1 au for Vega. Interior and exterior to ~ 4 au, this combined approach reaches planet detection limits down to $\sim 2\text{--}3 M_{\text{Jupiter}}$ using radial velocity and direct imaging, respectively.

Conclusions. By reaching multi-Jupiter mass detection limits, our results are expected to be complemented by the planet imaging of Vega in the upcoming observations using the *James Webb Space Telescope* to obtain a more holistic understanding of the planetary system configuration around Vega.

Key words. stars: imaging – planets and satellites: detection – techniques: high angular resolution – techniques: image processing – planets and satellites: individual: Vega

1. Introduction

Vega (α Lyrae, *Keoe*, *wāqi*¹, *Zhinü* 织女星), one of the historical photometric standard stars (Johnson & Morgan 1953), is an A0 V star (e.g., Johnson & Morgan 1953) that is located at 7.68 ± 0.02 pc from the Solar System (van Leeuwen 2007). Despite its proximity, Vega is not included in the *Gaia* Catalog of Nearby Stars that are within 100 pc from the Sun, since its brightness exceeds the *Gaia* limits (*Gaia* Collaboration et al. 2021). With an age of 445 ± 13 Myr (Yoon et al. 2010), Vega shows a prototypical mid-infrared excess in the *IRAS* observations, situating it in an evolutionary stage that is between star formation and our Solar System (Aumann et al. 1984).

The two-belt debris disk system around Vega may result from planet-disk interaction under various planetary configurations (e.g., Matrà et al. 2020). In fact, most existing directly imaged planets are found in bright debris disk systems (e.g., HR 8799: Marois et al. 2008, β Pic: Lagrange et al. 2009, 51 Eri: Macintosh et al. 2015), making it more likely to find giant planets in debris disk systems than around stars without disks (Meshkat et al. 2017). Combined with the observational fact that giant planets are more likely to exist at 1–10 au from their host stars in both direct imaging and radial velocity surveys (Nielsen et al. 2019; Fulton et al. 2021), the proximity of Vega makes it one of the best systems for giant planet search.

Before the resolved imaging of debris belts around Vega, dust structures around Vega have suggested the existence of potential planetary perturbers (e.g., Holland et al. 1998; Wilner et al. 2002) and called for deep imaging of them. Combining the Gemini Altair adaptive optics (AO) system and the NIRC instrument, Marois et al. (2006) obtain 5σ detection limits of better than 18 Mag at $3''$ – $10''$ in the off-methane $1.58\mu\text{m}$ 6.5% filter, or $\sim 3 M_{\text{Jupiter}}$ at $8''$. Using the MMT AO and the Clio camera, Hinz et al. (2006) and Heinze et al. (2008) obtain 10σ limits of better than ~ 12 Mag at $2''$ – $11''$ at M -band, or $\sim 10 M_{\text{Jupiter}}$.

Recent observational studies on the Vega planetary system are in direct imaging, transiting, radial velocity, and (sub)millimeter interferometric imaging. In direct imaging, Meshkat et al. (2018) presented observations from the coronagraphic integral field spectrograph P1640 at Palomar Observatory in J and H bands. Despite a non-detection of planets, they obtained 5σ planet detection limits from $0''.25$ to $2''$, reaching a best sensitivity of $\approx 20 M_{\text{Jupiter}}$ at $1''.5$ or 12 au. From a complimentary approach, using the Atacama Large Millimeter/submillimeter Array (ALMA), Matr a et al. (2020) observed and modeled the outer belt from ~ 60 au to ~ 200 au. To explain the observed disk architecture, Matr a et al. (2020) discussed three mechanisms which include a single giant planet, multiple low-mass planets, and no outer planets. Combining a decade of TRES spectra for radial velocity and two sectors of *TESS* photometry, and under the scenario that the planetary orbits have inclinations between $1^\circ 5$ and $11^\circ 5$, Hurt et al. (2021) obtained non-detection of 1– $10 M_{\text{Jupiter}}$ planets within 1–10 au, while reporting a candidate Jovian signal with a period of 2.43 day in radial velocity measurements. Nevertheless, depending on the orbit orientations of the planets, the mass limit can vary by up to a factor of ~ 10 in Fig. 6 of Hurt et al. (2021).

To improve existing high-contrast imaging limits, test different mechanisms for the formation of Vega debris disk system observed in ALMA, and explore beyond the nearly edge-on limitations from radial velocity and transit studies, we observed Vega in M_s -band using the vortex coronagraph on Keck/NIRC2. In M_s -band, planets have relatively larger planet-to-star brightness ratios than in J - or H -band (e.g., Spiegel & Burrows 2012; Skemer et al. 2014), and the advantage of M_s -band over shorter-wavelength bands improves for intermediate system ages for a planet of a given mass (e.g., Currie et al. 2022), both enabling us to explore around Vega for possible cooler and less massive planets than existing studies.

2. Observation and Data Reduction

We observed Vega using the Keck/NIRC2 vortex coronagraph in M_s -band in two individual nights using the narrow camera with a pixel size of 9.942 mas (e.g., Service et al. 2016; Mawet et al. 2019). The first observation is on UT 2018 August 30 under program C314 (PI: D. Mawet), the total integration time is 1991 s ($= 0.181 \text{ s} \times 100 \text{ coadds} \times 110 \text{ frames}$), and the parallactic angle change is $74^\circ 9$. The second observation is on UT 2019 August 20 under program N097 (PI: T. Meshkat), the total integration time is 4500 s ($= 0.25 \text{ s} \times 150 \text{ coadds} \times 120 \text{ frames}$), and the parallactic angle change is $81^\circ 6$. We list the observation details in Table 1.

Faint planetary signals are often overwhelmed by the stellar point spread function (PSF) of the central star. In order to remove the stellar PSF and reveal faint surrounding signals, we first preprocess the data using the VIP package (Gomez Gonzalez et al. 2017), which is further customized for NIRC2 vortex observations by performing flat-fielding, bad pixel and background re-

Table 1. Keck/NIRC2 vortex coronagraph observation log

Target	Vega	
Filter	M_s -band	
UT Date	2018 Aug 30	2019 Aug 20
UT Start	05:15:26.35	06:35:47.62
UT End	07:15:00.52	10:12:23.95
Airmass ^a	1.066 ± 0.009	1.159 ± 0.101
DIMM Seeing ^{a,b}	$0''.42 \pm 0''.11$	$1''.18 \pm 0''.55$
MASS Seeing ^{a,b}	$0''.16 \pm 0''.06$	$0''.18 \pm 0''.08$
Precipitable Water Vapor level	$\sim 7 \text{ mm}$	$\sim 2 \text{ mm}$
Parallactic Angle Change	$74^\circ 9$	$81^\circ 6$
Single Integration Time	0.181 s	0.25 s
Coadd For Single Frame	100	150
Total Frame Count	110	120
On-target Integration Time	1991 s	4500 s
Total On-target Time	1.803 h	
Pixel Scale	9.942 mas	

Notes: ^aThe uncertainties in this Letter are 1σ unless otherwise specified.

^bCalculated during this observation using

<http://mkwc.ifa.hawaii.edu/current/seeing/index.cgi>.

moval, and image centering (Xuan et al. 2018). We then reduce the preprocessed data using the Karhunen–Lo ve image projection algorithm (KLIP; Soummer et al. 2012; Amara & Quanz 2012) that performs principal component analysis to capture the stellar PSF and speckles in the observation. For an image, we remove its stellar PSF and speckles by first projecting it to the KLIP components, and subtract the projection from the original image to obtain the residuals. Astrophysical signals including planets and disks will then reside in these residuals. To obtain the final image for each observation, we obtain the residual maps for each individual readout, then rotate and median combine them.

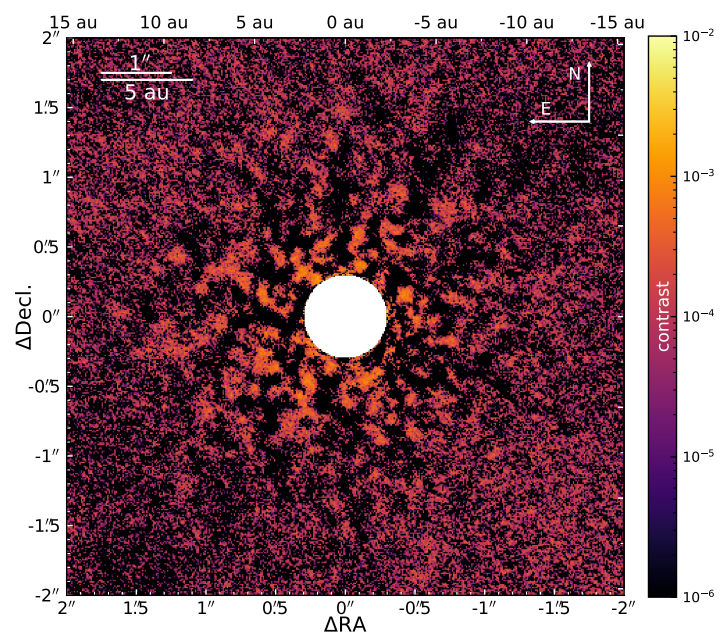


Fig. 1. Combined two-epoch NIRC2 image of Vega in M_s -band using ADI with 10% of the KLIP components for demonstration purposes. We do not identify point sources that are of more than 5σ levels beyond the noise of similar angular separation from the star. The pixel values correspond to lower limits of contrast values due to over- and self-subtraction with KLIP and ADI, respectively.

We present the combined two-epoch result using 10% of the KLIP components with angular differential imaging (ADI; Marois et al. 2006) in Fig. 1 for demonstration purposes, in which we do not identify point sources that are beyond 5σ of the noise that is within the same angular separation from the stars.

Using VIP and taking into account of self-subtraction and over-fitting with ADI while using KLIP, we generate the 5σ contrast limits for each observation following Xuan et al. (2018) by varying the reduction parameters to obtain the corresponding detection limits while performing corrections for small sample statistics in Mawet et al. (2014). Specifically, VIP performs injection recovery for companions at different locations to measure the throughput from ADI and KLIP (Gomez Gonzalez et al. 2017). In measuring our throughput, we inject companions along three radial branches spread throughout the image (originating from the masked center) where the averaged throughput at each radial location in the image is determined from these multiple estimates of the throughput at different branches (Xuan et al. 2018). We compute the contrast for the entire image for each combination of inner and outer mask size and number of principal components, where we compute up to 30 principal components. The ADI reduction is performed with no rotation gap; for one combination of inner and outer radii from Table 1 of Xuan et al. (2018), the full-frame reduction is performed on the an annulus zone with the region interior to the outer radius or exterior to the inner radius included (e.g., for an outer radius of $0''.5$ and an inner radius of $0''.08$, all pixels with radial separations between 8 pixel and 50 pixel from the center of the image, or between $0''.08$ and $0''.5$, are included in the reduction; see the reduction details in Xuan et al. 2018). While we do not use annular ADI, we do utilize the best contrast achieved from our full-frame ADI at each one pixel annulus.

To obtain the final detection limit, for each angular separation from the star with a step size of 1 pixel, we compare the detection limits from different combinations of reduction parameters. The reduction parameters including frame size (i.e., algorithmic inner and outer radii) and the number of principal components, see Sect. 2 and Table 1 of Xuan et al. (2018) for the details on how on computing most optimal contrasts using five different frame size combinations. Therefore, while our optimal contrast is the combination of frames processed using different parameters, we are optimizing at each radial location. For our observations, the number of principal components adopted for the final contrast curve ranges from 8 to 29, with a median of 15 and a standard deviation of 7.4.

The faintest companion that can be detected from such combinations at 5σ level is adopted as our final detection limit. For the 2019 data, the exposures that were used to image the unblocked central source were saturated, we thus fit the unsaturated first Airy ring to that of a theoretical model of the vortex stellar PSF (while taking into account of the PSF broadening effects due to weather by convolving a 2-dimensional Gaussian distribution), and use the best-fit model to generate the corresponding contrast curve. We then combine our detection limits from the two observations, and present them in Fig. 2. Although the 2018 observation has a shorter total on-target exposure time than the 2019 one, their total parallactic angle change difference is only $6^\circ.7$. With the DIMM seeing of $0''.41 \pm 0''.11$ in 2018 being more stable than that of $1''.18 \pm 0''.55$ in 2019, the 2018 data dominates the detection limits in the combined dataset.

3. Analysis

3.1. Mass detection limits

3.1.1. NIRC2 imaging

Being the photometric standard, Vega's apparent magnitude is defined as 0 in M_s -band. Adopting a distance of 7.68 ± 0.02 pc in van Leeuwen (2007), the absolute magnitude for Vega in M_s -band is 0.573 ± 0.006 .

With an age of 445 ± 13 Myr (Yoon et al. 2010) and adopting the AMES-Cond evolutionary models (Baraffe et al. 2003), we convert the contrast to 5σ mass detection limits in Fig. 2. We reach a detection limit of less than $5 M_{\text{Jupiter}}$ beyond 9 au, and $3 M_{\text{Jupiter}}$ beyond 14 au.

3.1.2. NIRC2 imaging and TRES radial velocity

Combining the 2018 NIRC2 results with the radial velocity data from the Tillinghast Reflector Echelle Spectrograph (TRES) in Hurt et al. (2021), we follow Hurt et al. (2021) to obtain the mass limits assuming the planetary orbits are well-aligned with the spin axis of Vega.

To explore the detectability of companions from both direct imaging and radial velocity measurements, we randomly generate 10^6 radial velocity samples of companion orbits following Hurt et al. (2021). The semi-major axis follows a log-uniform distribution ranging from 0.1 au to 22 au. The companion mass follows a log-uniform distribution ranging from 0.1 to $100 M_{\text{Jupiter}}$. The sine value of orbital inclination follows a uniform distribution from $1^\circ.5$ to $11^\circ.5$. The orbital eccentricity follows a beta distribution described in Kipping (2013). The argument of periastron follows a uniform distribution ranging from 0 to 2π radian. The time of periastron passage follows uniform distribution which is determined by the orbital period. The stellar mass follows a Gaussian distribution using the measurements from Monnier et al. (2012). In each radial velocity sample, we scale Gaussian noise according to the uncertainties of the TRES measurements in Hurt et al. (2021). We fit a flat line to each synthetic radial velocity curve using RadVal (Fulton et al. 2018).

For all simulated radial velocity samples, we consider a synthetic signal to be detectable in radial velocity, when its p -value < 0.001 (i.e., 3.3σ) while ignoring correlated noise (Hurt et al. 2021). At a specific radial separation from the star, we further require that a companion is detectable, when its mass is above the detection limit in Fig. 2.

We present the detection probability of companions from the above injection-recovery procedure in Fig. 3. The detectability of companions from combined radial velocity and direct imaging follows two trends as a function of stellocentric separation. Interior to ~ 4 au, the detectable planets increases with radial separation, approaching planets with $\sim 8 M_{\text{Jupiter}}$ down to $\sim 1 M_{\text{Jupiter}}$ at ~ 0.1 au. Exterior to ~ 4 au, the detectability is dominated by NIRC2 imaging, reaching down to $\sim 2 M_{\text{Jupiter}}$ at ~ 22 au. Under the Hurt et al. (2021) framework, there is a possible non-absolute detection of companions near ~ 22 au, which is limited by the NIRC2 field of view in our study, since the sampled orbital eccentricity adopted from Kipping (2013) can position planets with semi-major axis less than ~ 22 au beyond the 22 au angular radius.

3.2. Disk formation from mass limits

The ALMA observation in Matrà et al. (2020) resolves the outer dust belt of Vega extending from ~ 60 au beyond ~ 150 au.

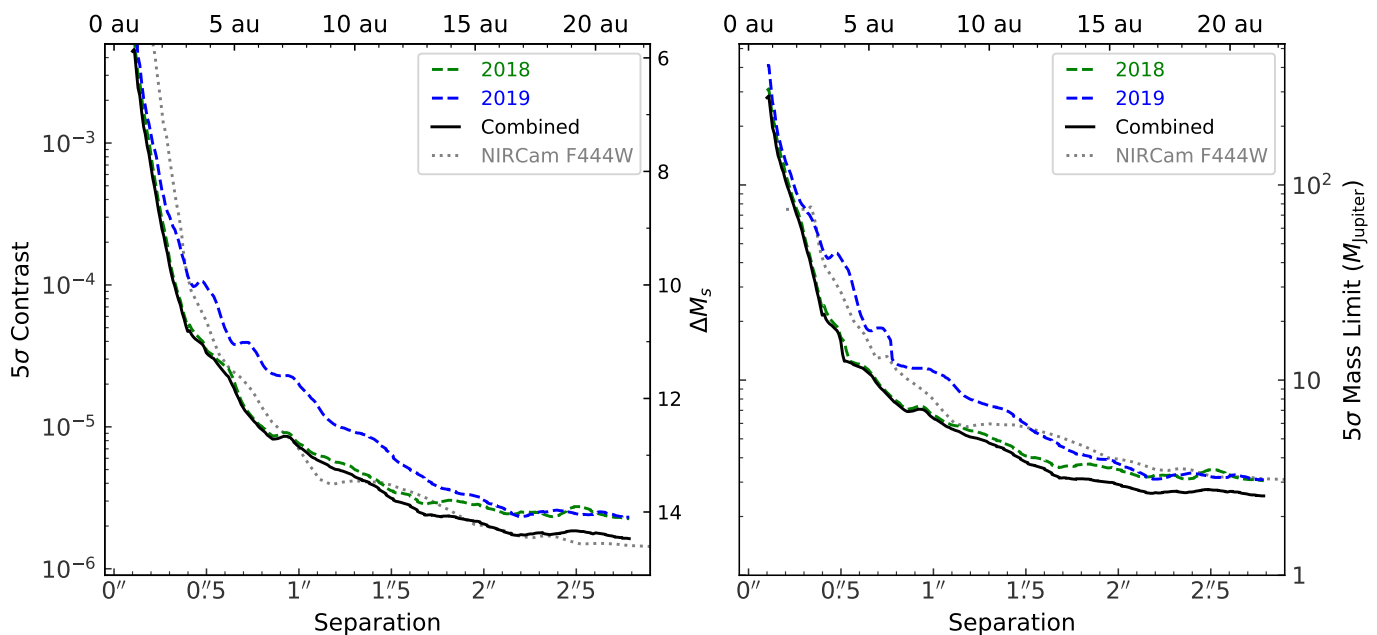


Fig. 2. Detection limits of point sources around Vega in M_s -band. Left: 5σ contrast, in comparison with *JWST*/NIRCcam F444W on-sky contrast calculated from Carter et al. (2022). Right: 5σ mass detection limit, and expected mass detection limit with NIRCcam F444W. Note: the NIRCcam F444W values have assumed identical instrument performance in the *JWST*/ERS-1386 program, see Sect. 3.3.

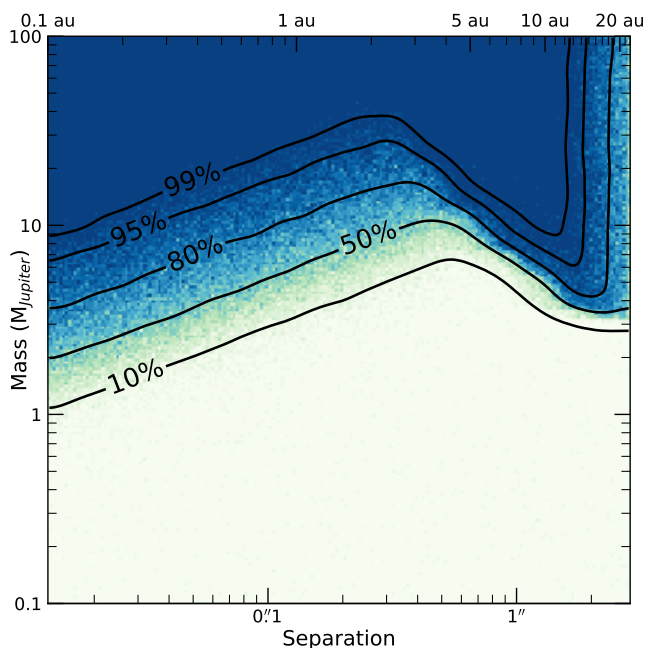


Fig. 3. Detection probability of point sources as a function of semi-major axis of points sources for Vega, using a combination of the 2018 NIRC2 observation and the TRES radial velocity measurements in Hurt et al. (2021), see Sect. 3.1.2. We can reach $\sim 8 M_{\text{Jupiter}}$ detection limit at ~ 4 au, while probing down to $\sim 2\text{--}3 M_{\text{Jupiter}}$ at 0.1 au and 22 au, respectively.

To explain the observed planetary system architecture, the authors have analyzed two scenarios that involves planets: either a chain of small planets within 70 au with mass $\geq 6M_{\oplus}$, or a sole $\sim 5 M_{\text{Jupiter}}$ at 50 – 60 au.

The combined Keck/NIRC2 M_s -band and TRES result can exclude the existence of $\sim 8 M_{\text{Jupiter}}$ planets from 0.1 au to 22 au. Despite the fact that with an age of ~ 400 Myr there is no clear

brightness difference between the hot-start and cold-start models (e.g., Spiegel & Burrows 2012), the observations presented here cannot rule out the sole giant planet which resides at 50 – 60 au in Matrà et al. (2020) for Vega.

For future exploration of the proposed sole giant planet at 50 au to 60 au using Keck/NIRC2 in M_s -band, a field of view that is between $6''.5$ and $7''.8$ is needed. With a pixel scale of 9.942 mas, this corresponds to a half-width between 654 pixel and 785 pixel, which exceeds the current 512 pixel half-width of the narrow camera for NIRC2 and thus not achievable. Alternatively, NIRC2 offers sampling setups that have pixel sizes of 20 mas or 40 mas, yet these setups are not feasible for M_s -band imaging due to the corresponding increased sky background. Nevertheless, the planned upgrades of the NIRC2 detector electronics may permit faster readouts to enable M_s -band imaging for such purposes.

To explore far separation imaging for Vega using existing configuration of NIRC2, either offsetting the vortex center away from the center (e.g., the observation of HR 8799 b using the Gemini Planet imager in Wang et al. 2018) of the NIRC2 narrow camera, or executing observations without the vortex coronagraph, could enable a half-width of 785 pixel to test the sole giant planet scenario. With this 1024×1024 pixel field of view, the minimum permitted readout time is 0.18 s^1 , which could enable a nearly identical exposure sequence in the 2018 dataset presented here. Given that extra parallactic angle change is needed to cover the entire field of view for these setups, they are beyond the scope of this study.

3.3. Implications for *JWST* observations

At an age of 445 ± 13 Myr for Vega (Yoon et al. 2010), giant planets with several Jupiter mass do not have clear brightness distinction between different formation models in M -band (e.g., Fig. 7 of Spiegel & Burrows 2012). For planets with less than

¹ <https://www2.keck.hawaii.edu/inst/nirc2/ObserversManual.html#Section2.4>

$\sim 5 M_{\text{Jupiter}}$, their brightness is expected to peak at $4 \mu\text{m}$ to $6 \mu\text{m}$ (e.g., Figure 6 of Spiegel & Burrows 2012).

To image planets that are brightest at these wavelengths, we have applied the Keck/NIRC2 M_S -band which operates at a central wavelength of $4.67 \mu\text{m}$ with a bandpass of $0.24 \mu\text{m}$.² In comparison, the NIRCcam instrument onboard the *JWST* can cover nearly half the expected brightest wavelengths with its F444W filter ($4 \mu\text{m}$ to $5 \mu\text{m}$).³ By reaching a multi-Jupiter mass limit for 10 au to 20 au within this study, and one Jupiter mass or better beyond 20 au with NIRCcam (Meshkat et al. 2018, Fig. 5 therein), we can combine Keck/NIRC2 and *JWST*/NIRCcam to reach the deepest planet detection limit to investigate the planetary architecture for the Vega system.

Using the on-sky *JWST*/NIRCcam F444W contrast curve from Carter et al. (2022) in the *JWST* ERS-1386 program (Hinkley et al. 2022), we calculate the expected on-sky contrast for Vega with NIRCcam F440W in Fig. 2 for *JWST* GTO-1193 observations as follows. Assuming an identical instrument performance, which is an optimistic estimation given that the *JWST* GTO-1193 uses MASK430R since it has a larger inner working angle – and thus lower throughput – than MASK335R in the *JWST* ERS-1386 observations in Carter et al. (2022), we scale the exposure times with SUB320 subarray (i.e., Observations 35 & 36) from the *JWST* GTO-1193 observations and recalculate the contrast based on exposure time difference. We then convert the *JWST*/NIRCcam F444W contrast to point source mass following Carter et al. (2021) for Vega while adopting the same age and apparent magnitude as for NIRC2.

In terms of reaching nominal contrast, the Keck/NIRC2 M_S -band observations perform better than NIRCcam F440W within $1''$ and reaching a similar quality in exterior regions. In terms of mass detection limits, the Keck/NIRC2 M_S -band observations performs systematically better than the NIRCcam F444W under optimistic assumptions above. In addition, the degradation of contrast close to the transmission near the edges of the the coronagraphic masks⁴ from MASK335R in *JWST* ERS-1386 to MASK430R in *JWST* GTO-1193 has been ignored. All three aspects demonstrate that the NIRC2 M_S -band observations presented here establish the deepest high-contrast imaging exploration of planetary companions for Vega in the probed regions. Nevertheless, we emphasize that NIRCcam should be better than NIRC2 for most other systems, since the study presented here should be the best case scenario for ground-based M_S -band imaging due to the brightness of Vega; for other targets that are fainter than Vega, they will have less favorable contrasts due to the relative background levels on the ground from NIRC2.

3.4. Planet detection towards 0.1 arcsec

To obtain a more general understanding of planetary existence, the detection of intermediate separation planets near $\sim 0.1''$ will likely yield the most discovery of planets (e.g., Nielsen et al. 2019; Fulton et al. 2021). In fact, for the detection of far-separation planets, existing direct imaging surveys equipped with extreme adaptive optics systems have experienced a degradation of contrast close to the central sources (e.g., Nielsen et al.

2019; Vigan et al. 2021; Xie et al. 2022). In comparison, for the detection of close-in planets, existing radial velocity surveys have less completeness for long orbital period planets (e.g., Wittenmyer et al. 2020; Fulton et al. 2021). As a result, in the detection probability map of companions for Vega in Fig. 3, there is a clear gap for middling separations.

To fill the gap, the concept of the vortex fiber nuller (VFN; Ruane et al. 2019; Echeverri et al. 2020) is designed to detect and characterize planets near and within $0.1''$. Using nulling interferometry in the near-infrared, VFN suppresses on-axis starlight while retaining off-axis companion light with acceptable loss, which increases the signal-to-noise ratio for companions and thus better enables their detection and characterization. The VFN is already installed on the phase 2 development of the Keck Planet Imager and Characterizer (KPIC; Jovanovic et al. 2020, Echeverri et al., in preparation) on the Keck Observatory, providing access to planets between 30 and 90 mas in K -band. Furthermore, the limitation of VFN in localizing the companions in their orbit will be further resolved with the concept of photonic lantern nuller (PLN; e.g., Xin et al. 2022). We expect that the application of VFN and PLN will fill the planet detection and characterization gap between direct imaging and radial velocity. For Vega, they will better explore possible hidden planets towards $\sim 0.1''$ in Fig. 3. Nevertheless, the limitation of VFN in K -band is that it is less sensitive to evolved and cooler giant planets due to the drop in planet brightness in shorter wavelengths.

4. Summary

We report 1.8 h of M_S -band imaging observations of Vega using the Keck/NIRC2 vortex coronagraph. Despite a non-detection of companions, we have pushed the mass detection limits from existing high-contrast imaging observations in Meshkat et al. (2018) by nearly an order of magnitude smaller, see Fig. 2. Combining the NIRC2 results with existing radial velocity study using TRES in Hurt et al. (2021), we can confidently rule out companions more massive than $\sim 8 M_{\text{Jupiter}}$ from 0.1 au to 22 au for Vega. Within this range, NIRC2 can reach planets that are less massive than $5 M_{\text{Jupiter}}$ beyond 9 au.

While the NIRC2 observations presented here are sensitive to planets of $5 M_{\text{Jupiter}}$ at 9 au down to $3 M_{\text{Jupiter}}$ at 22 au, it is limited by the field of view and thus cannot be used to test the scenario in Matrà et al. (2020) that one multi-Jupiter mass planet at 50 au to 60 au is responsible for the planetary system architecture. Alternatively, observing without using the vortex coronagraph while performing multi-point dithering⁵, combined with extra parallactic angle change, may provide enough sensitivity to image such a perturber for the Vega system by pushing deeper than Heinze et al. (2008) for these separations.

Combining Keck/NIRC2 in M_S -band and NIRCcam in its F444W filter assuming identical performance with *JWST* from ERS-1386 observations (Hinkley et al. 2022; Carter et al. 2022), we can reach comparable detection limits of companions interior to 20 au. Interior to ~ 10 au, although companion imaging limits increases from $\sim 5 M_{\text{Jupiter}}$ at 10 au to $\sim 100 M_{\text{Jupiter}}$ at 2 au in Fig. 2, this region is where radial velocity measurements can provide detection limits of multi-Jupiter or better in Hurt et al. (2021). Future works following Mawet et al. (2019) and Llop-Sayson et al. (2021) in combining measurements including direct imaging here and radial velocity in Hurt et al. (2021), as well as upcoming imaging observations with *JWST* GTO-1193, in ad-

⁵ <https://www2.keck.hawaii.edu/inst/nirc2/ObserversManual.html#Section3.2.10>

² <https://www2.keck.hawaii.edu/inst/nirc2/filters.html>

³ <https://jwst-docs.stsci.edu/jwst-near-infrared-camera/nircam-instrumentation/nircam-filters>

⁴ Fig. 3 of <https://jwst-docs.stsci.edu/jwst-near-infrared-camera/nircam-instrumentation/nircam-coronagraphic-occluding-masks-and-lyot-stops>

dition to the VFN and PLN concepts to detect planets towards $\sim 0''.1$, can enable us to obtain the most holistic understanding for the planetary system of this historical photometric standard star – Vega.

Acknowledgements. We thank the anonymous referee for their constructive comments that increased the clarity and reproducibility of this paper. This research is partially supported by NASA ROSES XRP, award 80NSSC19K0294. B.R. has received funding from the European Research Council (ERC) under the European Union’s Horizon 2020 research and innovation programme (PROTOPLANETS, grant agreement No. 101002188). É.C. has received funding from the European Research Council (ERC) under the European Union’s Horizon Europe research and innovation programme (ESCAPE, grant agreement No 101044152). Some of the data presented herein were obtained at the W. M. Keck Observatory, which is operated as a scientific partnership among the California Institute of Technology, the University of California and the National Aeronautics and Space Administration. The Observatory was made possible by the generous financial support of the W. M. Keck Foundation. The authors wish to recognize and acknowledge the very significant cultural role and reverence that the summit of Maunakea has always had within the indigenous Hawaiian community. We are most fortunate to have the opportunity to conduct observations from this mountain. Part of the computations presented here were conducted in the Resnick High Performance Computing Center, a facility supported by Resnick Sustainability Institute at the California Institute of Technology.

References

- Amara, A., & Quanz, S. P. 2012, *MNRAS*, **427**, 948
- Aumann, H. H., Gillett, F. C., Beichman, C. A., et al. 1984, *ApJ*, **278**, L23
- Baraffe, I., Chabrier, G., Barman, T. S., et al. 2003, *A&A*, **402**, 701
- Carter, A. L., Hinkley, S., Bonavita, M., et al. 2021, *MNRAS*, **501**, 1999
- Carter, A. L., Hinkley, S., Kammerer, J., et al. 2022, *arXiv*, [arXiv:2208.14990](https://arxiv.org/abs/2208.14990)
- Currie, T., Biller, B., Lagrange, A.-M., et al. 2022, *arXiv*, [arXiv:2205.05696](https://arxiv.org/abs/2205.05696)
- Echeverri, D., Ruane, G., Calvin, B., et al. 2020, *Proc. SPIE*, **11446**, 1144619
- Fulton, B. J., Petigura, E. A., Blunt, S., & Sinukoff, E. 2018, *PASP*, **130**, 044504
- Fulton, B. J., Rosenthal, L. J., Hirsch, L. A., et al. 2021, *ApJS*, **255**, 14
- Gaia* Collaboration, Smart, R. L., Sarro, L. M., et al. 2021, *A&A*, **649**, A6
- Gomez Gonzalez, C. A., Wertz, O., Absil, O., et al. 2017, *AJ*, **154**, 7
- Heinze, A. N., Hinz, P. M., Kenworthy, M., et al. 2008, *ApJ*, **688**, 583
- Hinkley, S., Carter, A. L., Ray, S., et al. 2022, *PASP*, **134**, 095003
- Hinz, P. M., Heinze, A. N., Sivanandam, S., et al. 2006, *ApJ*, **653**, 1486
- Holland, W. S., Greaves, J. S., Zuckerman, B., et al. 1998, *Nature*, **392**, 788
- Hurt, S. A., Quinn, S. N., Latham, D. W., et al. 2021, *AJ*, **161**, 157
- Johnson, H. L., & Morgan, W. W. 1953, *ApJ*, **117**, 313
- Jovanovic, N., Calvin, B., Porter, M., et al. 2020, *Proc. SPIE*, **11447**, 114474U
- Kipping, D. M. 2013, *MNRAS*, **434**, L51
- Lagrange, A. M., Gratadour, D., Chauvin, G., et al. 2009, *A&A*, **493**, L21
- Llop-Sayson, J., Wang, J. J., Ruffio, J.-B., et al. 2021, *AJ*, **162**, 181
- Macintosh, B., Graham, J. R., Barman, T., et al. 2015, *Science*, **350**, 64
- Marois, C., Lafrenière, D., Doyon, R., et al. 2006, *ApJ*, **641**, 556
- Marois, C., Macintosh, B., Barman, T., et al. 2008, *Science*, **322**, 1348
- Matrà, L., Dent, W. R. F., Wilner, D. J., et al. 2020, *ApJ*, **898**, 146
- Mawet, D., Milli, J., Wahhaj, Z., et al. 2014, *ApJ*, **792**, 97
- Mawet, D., Hirsch, L., Lee, E. J., et al. 2019, *AJ*, **157**, 33
- Meshkat, T., Mawet, D., Bryan, M. L., et al. 2017, *AJ*, **154**, 245
- Meshkat, T., Nilsson, R., Aguilar, J., et al. 2018, *AJ*, **156**, 214
- Monnier, J. D., Che, X., Zhao, M., et al. 2012, *ApJ*, **761**, L3
- Nielsen, E. L., De Rosa, R. J., Macintosh, B., et al. 2019, *AJ*, **158**, 13
- Ruane, G., Echeverri, D., Jovanovic, N., et al. 2019, *Proc. SPIE*, **11117**, 1111716
- Service, M., Lu, J. R., Campbell, R., et al. 2016, *PASP*, **128**, 095004
- Skemer, A. J., Marley, M. S., Hinz, P. M., et al. 2014, *ApJ*, **792**, 17
- Soummer, R., Pueyo, L., & Larkin, J. 2012, *ApJ*, **755**, L28
- Spiegel, D. S., & Burrows, A. 2012, *ApJ*, **745**, 174
- van Leeuwen, F. 2007, *A&A*, **474**, 653
- Vigan, A., Fontanive, C., Meyer, M., et al. 2021, *A&A*, **651**, A72
- Wang, J. J., Graham, J. R., Dawson, R., et al. 2018, *AJ*, **156**, 192
- Wilner, D. J., Holman, M. J., Kuchner, M. J., & Ho, P. T. P. 2002, *ApJ*, **569**, L115
- Wittenmyer, R. A., Wang, S., Horner, J., et al. 2020, *MNRAS*, **492**, 377
- Xie, C., Choquet, E., Vigan, A., et al. 2022, *A&A*, **666**, A32
- Xin, Y., Jovanovic, N., Ruane, G., et al. 2022, *ApJ*, **938**, 140
- Xuan, W. J., Mawet, D., Ngo, H., et al. 2018, *AJ*, **156**, 156
- Yoon, J., Peterson, D. M., Kurucz, R. L., & Zagarelio, R. J. 2010, *ApJ*, **708**, 71